Low-Temperature Deformation Mechanism and Strain-Hardening Behaviour of Laser Welded Dual-Phase Steels

Isiaka Aderibigbe [1],*, Patricia Popoola [1], Emmanuel Sadiku [2] and Elliot Biro [3]

1 Department of Chemical and Metallurgical Engineering, Tshwane University of Technology, Pretoria 0183, South Africa
2 Department of Polymer Technology, Tshwane University of Technology, Pretoria 0001, South Africa
3 Department of Mechanical and Mechatronics Engineering, University of Waterloo, Waterloo, ON 2NL 3G1, Canada
* Correspondence: ia.aderibigbe@gmail.com

Abstract: This paper analysed the change in microstructure after laser welding DP800 and DP1000, the effect of the laser welds on low temperatures deformation, and strain hardening behaviour when loaded at temperatures between $-40\ ^\circ$C and 20 $^\circ$C using quasi-static strain rates ($1.7 \times 10^{-2}\ \mathrm{s}^{-1}$). The results showed that the fusion zone (FZ) was fully martensitic due to the rapid cooling during welding. Owing to the severity of the heat-affected zone, the joint efficiencies of DP800-DP800 and DP1000-DP1000 welds were 99.0% and 88.7%, respectively. The UTS, YS, and work hardening exponents of the welded joints increased slightly, while the strain hardening capacity of the base metals was much higher than those of the welded joints with decreasing temperatures. The evaluated work hardening exponents of the welded joints were determined using the Hollomon equation, Afrin equation, and Crussard-Jaoul analysis are in the range of 0.2–0.47, 0.24–0.59, and 0.45–0.71, respectively. The welded joints and the base metals demonstrated only stage III strain hardening, with DP800 joints exhibited excellent uniform and total elongation ranging between 8.0–8.7% and 10.4–14.2%, respectively. Fractures were located in the base metal of welded DP800 and SCHAZ of DP1000 welds, respectfully. The fracture surfaces demonstrated characteristic dimple fractures. The uniqueness of this study is found in its design, as there is currently no known literature on the low-temperature deformation mechanism and strain-hardening behaviour of similar DP800 and DP1000 welds.

Keywords: dual phase (DP) steels; strain hardening; laser welding; low temperatures; dislocation density; plasticity

1. Introduction

To reduce the environment footprint of automobiles, automotive manufacturers are adopting designs to reduce CO_2 emissions through improved fuel economy. As part of this effort, the automotive industry has been driven to adopt lighter, yet stronger materials to reduce vehicle weight without compromising occupant safety. One example of such materials is dual phase (DP) steel, which is a type of advanced high strength steel (AHSS), commonly used in automotive industries. These steels have a multiphase microstructure made of ferrite, martensite, and sometimes bainite and pearlite [1,2]. As a result of its multiphase microstructure, this steel possesses a unique combination of mechanical properties, which include: good ductility, continuous yielding behaviour, high tensile strength, and initial high work hardening rate during plastic deformation, all of which give it advantages over conventional low carbon and high strength low alloy steels (HSLA) [3–5]. Specifically, it has been shown that the high strain hardening rates in dual phase steels are attributed to the hard martensitic structure distributed in the ferritic matrix [6]. Additionally, the ductility of DP steel is improved by the soft ferrite matrix, while the islands of martensite particles contribute to the strength by allowing for a pile-up of dislocations on the martensitic boundaries, leading to kinetic hardening [1,7–9]. The higher initial work

hardening rate results in their good formability and crash worthiness properties which found use in the automotive industries [10,11].

Lasers are invaluable in modern-day manufacturing industries, as they are used to solve a variety of problems and enhance production through rapid prototyping, geometrical freedom, and customization [12]. To join DP steels during automotive construction, various welding techniques, such as gas metal arc welding (GMAW), friction stir welding (FSW), resistance spot welding (RSW), and laser beam welding (LBW) [13–15], have been applied in the automobile industry. Laser welding is gaining acceptance due to its high efficiency and flexibility [16]. In high strength welding applications such as the oil industry, gas pipelines, and shipbuilding, it is well known that weld mechanical properties of high strength steels are strongly influenced by temperature. This is especially true for welds in these materials where there is severe grain growth in the coarse grain heat-affected zone (HAZ), which will exasperate brittle at sub-zero temperatures, as reported by Uemori et al. [17].

Several studies have been conducted that related the mechanical properties and strain hardening characteristics of DP steels to its microstructure. It has been shown that the tensile characteristics of these steels depend on the volume fraction of the constituent phases [18,19], strain rate [20,21], strength [1], and martensite morphology [22,23], etc. Several authors have applied constitutive model laws of stress–strain correlation to describe the deformation hardening behaviour of DP steels [18,24–26]. The most common laws include: Cock-Mecking type [27], Hollomon analysis [28], and Crussard-Jaoul (C-J) analysis [29,30] premised on Ludwik [31] and Swift (Swift, 1952) equations [32], commonly referred to as C-J (DC-J) [33,34], commonly referred to as C-J (DC-J) and modified C-J (MC-J) methods [35,36], respectively. The models that describe the flow stress dependence on the temperature and the strain rate include: Hollomon's, Johnson–Cook, and Preston–Tonks–Wallace [37]. In the current study, the plasticity models that are used include: Hollomon's power law, C-J analysis, and Afrin model. The advantages/practical use of each model are summarized in Table 1.

The ambient and high-temperature mechanical behaviour of welded DP steels are well known in both quasi-static and dynamic conditions [38]. In a recent study by [38], it was found that the strength of the as-received DP600 steel increased markedly as the strain rate increased above those used in quasi-static tests; however, this study was carried out at ambient temperatures. Similar results were reported by [39] after conducting tensile tests at different strain rates between 10^{-4} to 10^2 s^{-1} and deformation temperature between -60 to $100\,^\circ$C on DP800 base metal. The authors reported an increase in the yield (YS) and the ultimate tensile strength (UTS) of the steel with increasing strain rate and as temperature decreased. Similar findings have been reported by other researchers [40–42].

There are other grades of AHSS than DP steels that are used in different parts of body-in-white (BIW) of automobiles, such as boron steel, which has the highest strength, used for passenger compartment zone due to their higher crashworthiness property [43]. Other critical parts of the BIW are still dominated by DP800 and DP1000 steels due to their good crashworthiness properties. For example, DP800 could be applied in axial crush regions (i.e., B-pillar) while DP1000 is used for the protective cabin structural parts (i.e., side rail) [43]. Considering this, there have been a lot of studies focusing on the microstructure and mechanical characteristics of welded similar DP800-DP800 and DP1000-DP1000 [44–46]. However, there is no report on the tensile properties and deformation behaviour of the welded joints of DP800 and D1000 steels at low temperatures, which is important to investigate, considering the hash environmental conditions at low temperatures to which vehicles are exposed in cold climate regions. The main contribution of this study is the analysis of tensile behaviour of two welded commercial DP steels at sub-zero temperatures for automotive applications. The reason why this research is focused on low temperatures (i.e., 0 °C to −40 °C) is because low temperature data of DP steels are scarce in the literature, and it is very important to understand the tensile behaviour of these grades at sub-zero temperatures as they are used for several safety critical compo-

nents in the automobiles used in cold regions with similar ranges of low temperatures. These findings would help to provide needed data on the tensile behaviour of welded DP steels at low temperatures and provide recommendations on how the properties can be optimized to ensure safe design of vehicles for low temperature applications.

The results are compared to room temperature characteristics. Special attention is given to the fracture behaviour. Therefore, this study is aimed at evaluating the tensile characteristics and strain hardening behaviour of laser welded DP800 and DP100 joints as well as the failure mechanism at different low deformation temperatures.

Table 1. Advantages/practical use and disadvantages of the models used in this work.

Plasticity Model	Advantages/Practical Applications	Disadvantages
(1). Hollomon Power Law	(1). The Hollomon model is most accurate for metals that have a strain-hardening coefficient between 0.1 and 0.3 [47,48]. (2). It is a straightforward mathematical model that can precisely describe the hardening characteristics of a material [49,50].	(1). The major limitation of the Hollomon equation is the assumption that the steel exhibited constant hardening exponent (n) throughout the entire tensile test. i.e., it is limited to describing only one deformation mode [51].
(2). Crussard-Jaoul	(1). C-J model can be used to analyse multistage hardening behaviour [52]. (2). C-J analysis results are independent of the level of flow stress. (3). C-J is the most commonly applied model for DP steels [52,53].	(1). A limitation of the C-J model is that the values of the constants in the equation depend on where the power law curve fits a range of experimental data and intercepts the strain axis [54]. (2). The model is not used in numerical simulations of sheet metal stamping processes. (3). C-J analysis results are significantly influenced by the pre-strain and manufacturing history of the material [54].
(3). Afrin model	It provides a rough estimate of hardening capacity of a material.	It does not express the exact hardening capacity.

2. Materials and Methods

The work in the current study was carried out on a 1.6-mm-thick DP800 with 70 g/m^2 galvannealed coating and a 1.2-mm-thick DP1000 with 75 g/m^2 galvannealed coating. The chemical compositions of the base metals (BMs) are presented in Table 2. The carbon equivalents (CE_Y) for the steels were determined using Yurioka's formula [55] as shown in Equation (1). The CE_Y is used to predict steel's weldability and to establish criteria to predict cold cracking in the HAZ, as they can predict HAZ hardenability.

$$CE_Y = C + f(C)\left[\frac{Si}{24} + \frac{Mn}{6} + \frac{Cu}{15} + \frac{Ni}{20} + \frac{(Cr + Mo + Nb + V)}{5}\right] \qquad (1)$$

where $f(C)$ = 0.75 + 0.25tanh [20(C-12)]. The mechanical properties of as-supplied base metals were given by the material supplier as part of standard manufacturing product characterization, they are shown in Table 3. Welding was performed using a Nd:YAG laser. Welding trials were performed by carrying out bead on plate on the steels to determine optimum laser parameters to produce maximum weld penetration and minimum bead width. It was found that the same optimum laser parameters were sufficient to successfully weld the two steel grades after the tested parameters produced good appearance, stability, maximum weld penetration, and minimum bead widths. The optimum welding parameters used for this investigation are shown in Table 4. A fibre-coupled 4.4 kW, CW diode pumped Rofin Sinar Nd:YAG laser mounted on a Panasonic VR6 robotic arm was used. A Precitec YW50 welding head was used and the laser beam was delivered through a 400 μm core diameter fibre. The laser beam was delivered perpendicular onto the surfaces to be welded with the focal point on the top surface thereof. A 200 mm collimator was used, together

with a 200 mm focal length lens, resulting in a 0.4 mm laser spot diameter, which was measured using D4σ technique.

Table 2. Chemical composition, coating characteristics, and CE of the investigated DP800 and DP1000 steels.

Steel Grade	C	Mn	Si	Al	Cr + Mo	Nb + Ti	Cu	Coating (g/m^2)	f_{mart} (%)	CE	Grain Size
DP800	0.15	1.8	0.01	0.015	-	0.1	-	70	41	0.26	6.7
DP1000	0.23	2.7	0.01	0.015	1.0	0.15	0.2	75	47	0.29	4.1

Table 3. Tensile properties of the base metals.

Steel Grade	DP800 BM	DP1000 BM
Yield strength (MPa)	560	780
UTS (MPa)	827	1040
Total Elongation (%)	16.6	11.5

Table 4. Laser parameters used for welding.

Laser System	Laser Source	Power (kW)	Wavelength (μm)	Beam Size (mm)	Focal Length (mm)	Welding Speed (m/min)
YW 50	Nd:YAG	4.4	1.06	0.4	200	4.5

Reprinted with permission from Ref. [56]. 2022, with the permission of the Laser Institute of America.

The samples edges were machined before welding to remove all gaps. Thereafter, the coupon was mounted and clamped on the welding table while the machined edges were firmly fitted together to prevent shifting or misalignment during welding. Shielding gas was used to protect the welds against oxidation from atmospheric contamination. Argon gas with a flow rate of 10 L/min was used for shielding on both sides of the blank during the welding process and was directed perpendicular to the welding direction while the gas nozzle moves concurrently together with the laser beam to ensure adequate shielding of the weld pool. The laser power output used for the welding was 4.4 kW while the welding speed was kept constant at 4.5 m/min. Welding was performed normal to the base metals rolling direction. The joining was performed in keyhole mode and the selected welding parameters achieved full penetration.

Metallographic samples of the welded joints were sectioned perpendicularly to the welding direction at about 25 mm from the blank edge to prevent the effects of welding instability and were prepared using the standard metallographic procedure and polished to a 1 μm diamond finish. Thereafter, the samples were etched using a 5% Nital solution for 2 s to reveal the microstructure. Subsequently, the specimens were observed with an optical microscope (OM, OLYMPUS DP72) and a scanning electron microscope (JEOL JSM 6460). Microstructural volume fractions and grain size were determined using ImageJ analysis software

Vickers microhardness measurements were made on the etched specimens according to ASTM E92-17 standards (2017) [56] with Future-Tech FM-700 hardness tester using a load of 500 g and a dwell time of 10 s. The hardness profile was traversed across the weld through the zones for all samples; the space between each indentation was 0.2 mm to ensure that strain fields from neighbouring indents did not interfere with each other. The tolerance associated with the average microhardness represents the standard deviation of the three measurements.

The laser welding setup and sample geometry are shown in Figure 1a. The tensile tests were carried out using sub-sized specimens machined to ASTM-E8M specifications Figure 1b. An Instron 5985 with an environmental chamber, fed by liquid Nitrogen was used

for tensile testing. Non-ambient tensile testing (NATT) was conducted at low temperatures between 20 °C to −40 °C. To ensure that the coupon reached the desired temperature, it was soaked in the chamber for about 10 min. After soaking, the coupon was then pulled at a low strain rate of 1.7×10^{-2} s^{-1}. The coupon gauge length of 25 mm and a non-contact AVE 2 extensometer was used to measure the strain. The 0.2% offset YS, UTS, ductility (total and uniform elongations), and the strain hardening rate were evaluated. The tensile fracture surfaces of the welded joints were examined using a scanning electron microscope (JEOL JSM 6460) equipped with an Oxford energy dispersive X-ray spectroscopy (EDS) system.
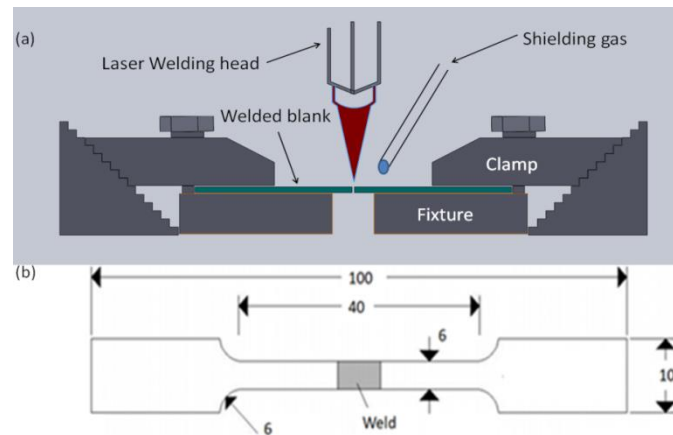

Figure 1. Illustrative schematics of (**a**) welding setup, and (**b**) ASTM E8 tensile sample geometry for Quasi-Static Tests (Dimensions are in mm).

3. Results and Discussion

3.1. Microstructural Evolution

Figure 2a,b present the light optical images of the cross-section of the laser DP800-DP800 and DP1000-DP1000 welded joints. The micrographs of the base metals are shown in Figure 3a,f. The microstructure of DP800 and DP1000 base metals contained a network of martensite islands in the ferrite matrix. The average grain size of the DP800 and DP1000 base metals determined with ImageJ analysis were 6.7 and 4.1 µm, respectively, measured along the rolling direction. It is noteworthy that the observed volume fraction of martensite in DP800 was lower compared with DP1000. The results obtained from ImageJ analysis showed that DP800 BM exhibited a 41% volume fraction of martensite while DP1000 steel contained a 47% martensite volume fraction.

After welding, a significant change can be seen in the microstructures across the joints. In the FZ, the peak temperature exceeds the steels' melting temperature and exhibits non-equilibrium solidification during cooling from the molten state. This can be correlated to the fast-cooling rate and concentrated heat input associated with laser welding. The solidification characteristic of the FZ exhibits epitaxial mechanism. For example, the solidification begins at the FZ/HAZ boundaries and progressively advances toward the weld centerline. The FZ microstructures were predominantly martensite (Figure 3e,j). Again, the martensite formation in the FZ was due to the fast cooling associated with the laser beam welding technique. It is significant to note that the HAZ micro-constituents of the steels i.e., ferrite and martensite were finer compared the unwelded samples as well as the FZ (Figure 3a–j). This can be correlated to the incomplete austenizing in the HAZ of the steels, even when there is presence of austenite grains; grain growth is limited due to the effects of thermal cycle and martensite formation [13]. However, the HAZ grains are finer, consequently leading to high density grain boundaries, and ultimately hindering the formation of large lath martensitic structures. Overall, the FZ microstructure of welded DP steels, as common to other AHSS, is influenced mainly by two factors: (1) the steel chemistry (i.e., carbon content and other alloying constituents), and (2) the cooling rates.
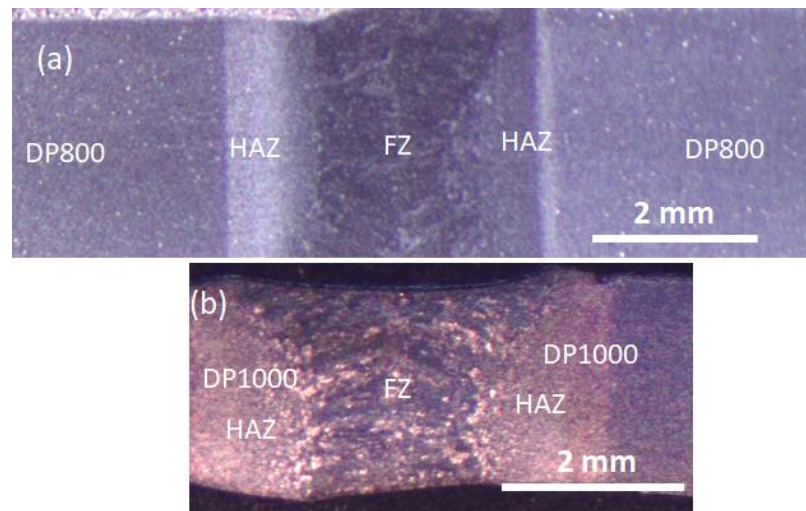
Figure 2. (**a**,**b**) light optical micrographs of the cross-sections of the DP800-DP800 and DP1000-DP100 welded joints.

The HAZ of the welded steels can be broadly categorized into four regions, i.e., the CGHAZ, FGHAZ, ICHAZ, and SCHAZ. The peak temperature in the softened HAZ was similar to or less than the critical temperature (A_{C1}, where austenite starts to form at elevated temperature) during welding, resulting in a tempering effect, and ultimately causing the existing martensite in the BM to degrade [57].

Figure 3b,g show the cross-section overview of the optical microstructure (OM) of the HAZ regions of welded DP800 and DP1000, respectively. The CGHAZ (Figure 3b,g) lies adjacent to the fusion zone. Although the peak temperature in this region is reasonably high compared to the FZ, it is characterized by a slower cooling rate, consequently resulting in grain growth of prior austenite upon cooling, and ultimately forming coarser martensite phase in the region. In the FGHAZ region, although austenite phase transition occurs during welding, it is common knowledge that the peak temperature is lower compared to that of CGHAZ, and austenite grain growth is generally more moderate than in the CGHAZ, causing the final microstructure to consist of fine equiaxial ferrite grains and a small amount of martensite, as shown in (Figure 3b,g). The intercritical HAZ (ICHAZ) experienced peak temperatures above Ac_1 but below the steel Ac_3 temperature, i.e., it consists of the region in the weld bounded by A_{C3} and A_{C1}. The microstructure in this region exhibits partially re-austenized grains and contains ferrite and tempered martensite (Figure 3d,i). The SCHAZ is the region that lies next to the unaffected base metal, where the peak temperature is below the steel's Ac_1 temperature of the steel [58]. The SCHAZ of DP800- and DP1000-welded joints are shown in (Figure 3c,h). The final microstructure in this region consists of tempered martensite (TM) and ferrite. The severely decomposed martensite phase is often referred to as the softened zone. Furthermore, it was seen that the tempered martensite in this region shows the presence of several sub-micron sized particles as indicated by the white arrows (Figure 3c,h), which can be attributed to the nucleation and growth of carbides [17].
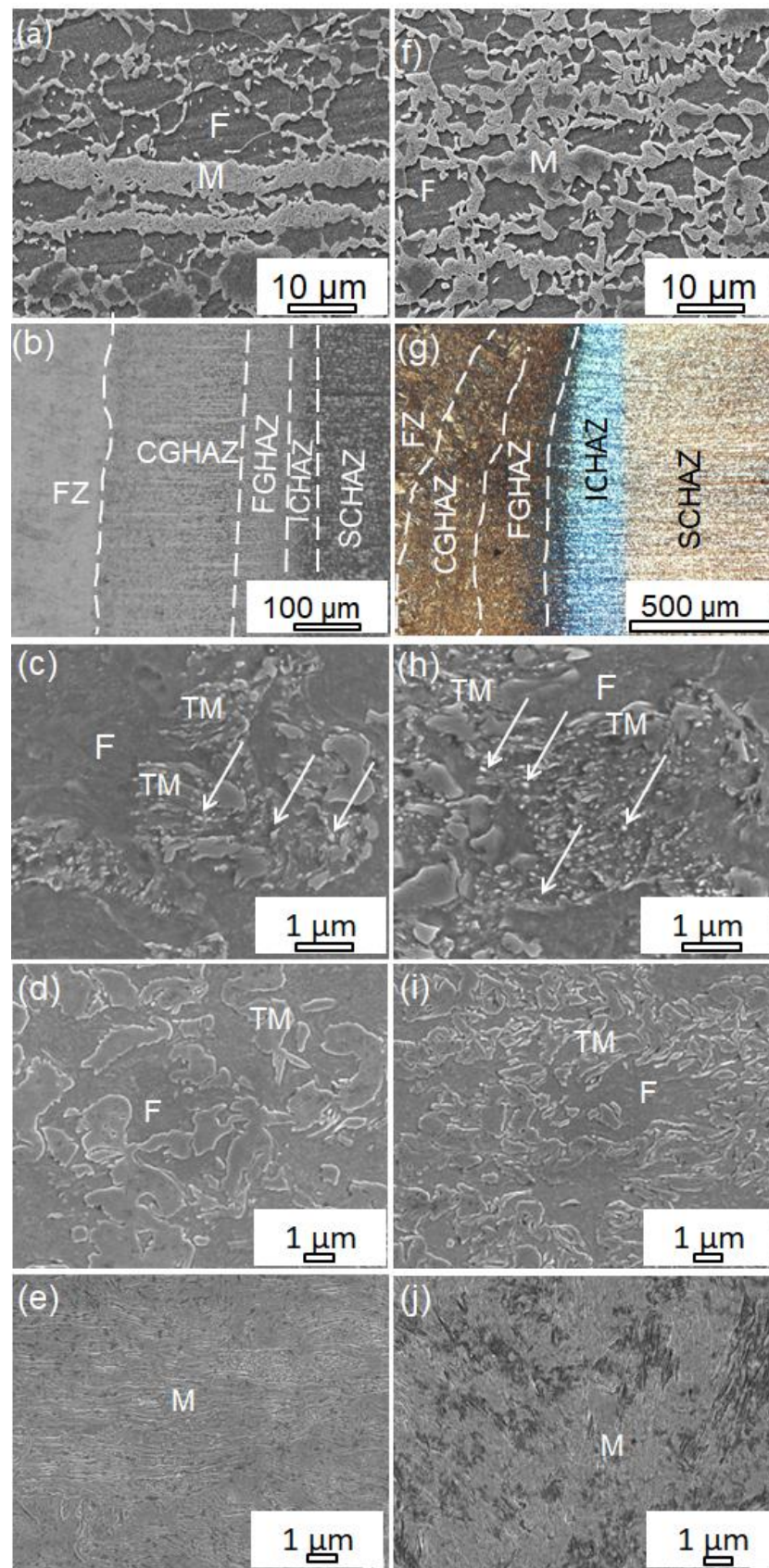
Figure 3. SEM and optical micrographs of welded DP800 joint: (**a**) BM; (**b**) Overview of HAZ; (**c**) SCHAZ; (**d**) ICHAZ; (**e**) FZ; and welded DP1000 joint: (**f**) BM; (**g**) Overview of HAZ; (**h**) SCHAZ; (**i**) ICHAZ; (**j**) FZ.

3.2. Microhardness

Figure 4a,b show the microhardness profiles of laser welded DP800 and DP1000 steel joints, respectively. It was seen that the respective measured fusion zone's hardness was substantially higher than their respective base metals (Figure 4a,b). Specifically, the FZ hardness was approximately 1.6 and 1.3 times higher than the DP800 and DP1000 base metals, respectively, which is correlated to the predominantly martensitic structure formed in the fusion zones. With regards to DP800-welded joint, the FZ hardness value was observed to be slightly higher than that in the DP1000-welded joint. As seen in Figure 4a,b, a softened zone can be seen in the microhardness profiles of both welded joints. The decrease in welded DP800 HAZ hardness was less than the hardness decrease exhibited in the HAZ hardness of DP1000 welded joint. The softening experienced in these zones has been attributed to partial disappearance and tempering of pre-existing martensite [58–60] as shown with the blue circles in Figure 4a,b. The difference between the softening exhibited by the DP800 and DP1000 can be attributed to the high martensite volume fraction in the DP1000 [58]. In addition, the HAZ width of DP800 joints (1.2 mm) is less than that of DP1000 joints (1.4 mm) (Figure 4); this is also correlated to the high martensite volume fraction in the DP1000 BM.
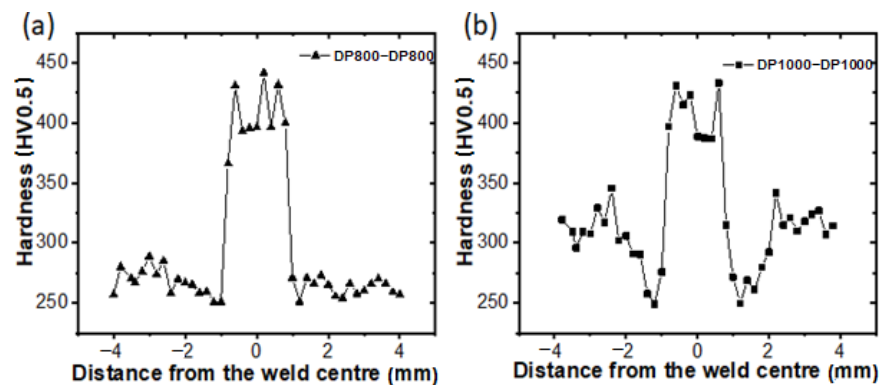

Figure 4. Microhardness profile of the laser-welded (**a**) DP800-welded joint and (**b**) D1000-welded joint.

3.3. Tensile Properties

The engineering stress–strain curves of the base metals, DP800 and DP1000 tested at different deformation temperatures of (a) 20 °C, (b) 0 °C, (c) −20 °C, and (d) −40 °C, at a quasi-static strain rate of 1.7×10^{-2} s^{-1} are presented in Figure 5, while those of the welded joints are shown in Figure 6. Figure 7a,b shows the effects of the welding cycle on the YS and UTS while the fractured samples are presented in Figure 8. The joint efficiencies of DP800-DP800 and DP1000-DP1000 welds were 99.0% and 88.7%, respectively, where the joint efficiency can be defined as the ration of the UTS of the weld joint to the UTS of the BM. It is seen that the base metals of DP800 and DP1000 as well as the welded joints (Figures 5 and 6) exhibit smooth and continuous plastic flow at all deformation temperatures due to mobile dislocations in the ferritic matrix during the tension test [59]. The welded samples showed no obvious yield point in the stress–strain curves, which agree with earlier results in the literature [61,62]. The UTS of the similar welded DP800 and DP1000 joints were found to range between 819–841 MPa and 922–959 MPa, respectively, and the YS between 419–629 MPa and 664–782 MPa (Figure 7a,b, respectively. Looking further in-depth into the data (Figure 7a), it is noteworthy that DP1000 BM exhibited the highest drop in UTS (28.9%) but a moderate drop in YS (5.4%) at 0 °C, compared to the drop in DP800 base metal UTS (7.6%) but with a greater decrease in YS (10.1%), respectively (Figure 7a,b).
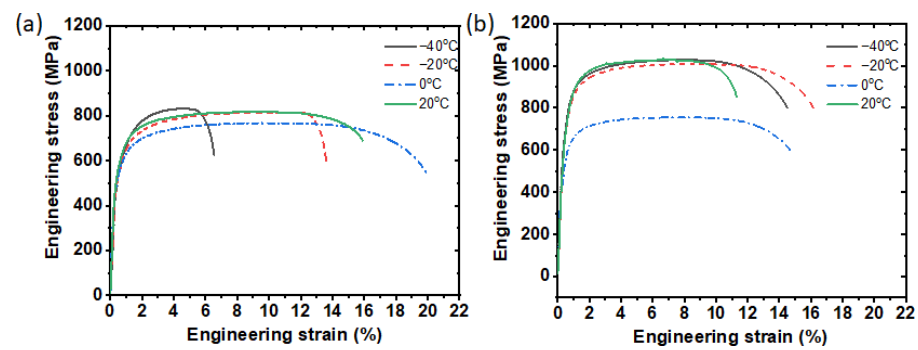
Figure 5. Engineering stress−strain curves of (**a**) DP800 and (**b**) DP1000 BM at different deformation temperatures of −40 °C. to 20 °C.
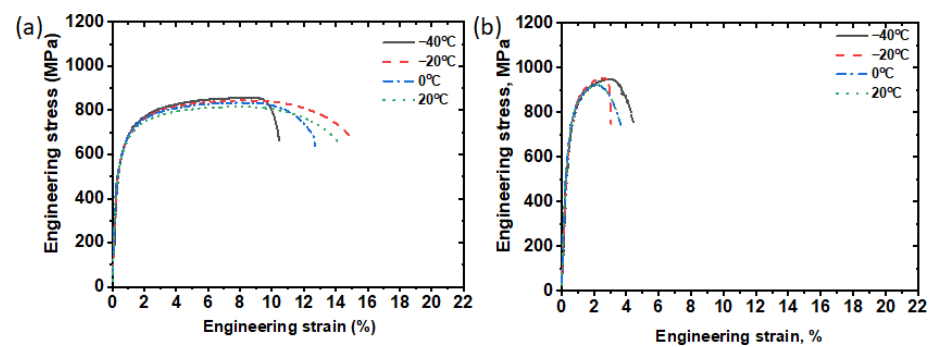

Figure 6. Engineering stress–strain curves of (**a**) DP800- and (**b**) DP1000-welded joints at different deformation temperatures.
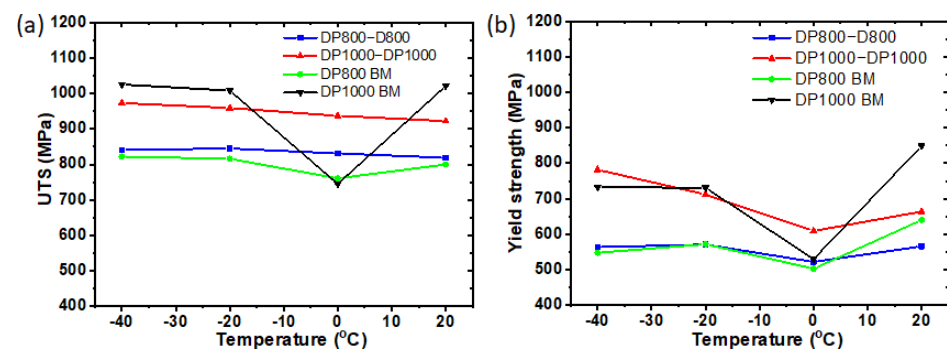
Figure 7. (**a**) UTS and (**b**) YS of base metals and welded DP steels at different deformation temperatures from −40 °C to 20 °C.

The difference in temperature-dependent mechanical strength may be due to higher effects of sudden onset of martensitic transformation experienced in welded DP1000 BM, since it has a higher volume fraction of martensite than DP800 base metal and welded DP800 and DP1000 joints, due to their degraded martensitic contents after welding (Figure 3c,h). Conversely, the YS of DP800 base metal and DP800-welded joint showed progressive increases in strength with decreasing deformation temperatures (Figure 7b). In summary, both the YS and UTS the base metals, and the welded joints showed marginal temperature sensitivity, with the strength increasing by a very small amount. For example, the UTS of welded DP800 and DP1000 increased between 1.5–2.7% and 1.6–5.5%, respectively, with decreasing temperatures, which correlates to the delayed dislocation movement at lower temperatures due to the reduced kinetic vibrations in the lattice, resulting in increased YS and UTS (except at 0 °C), as earlier discussed.
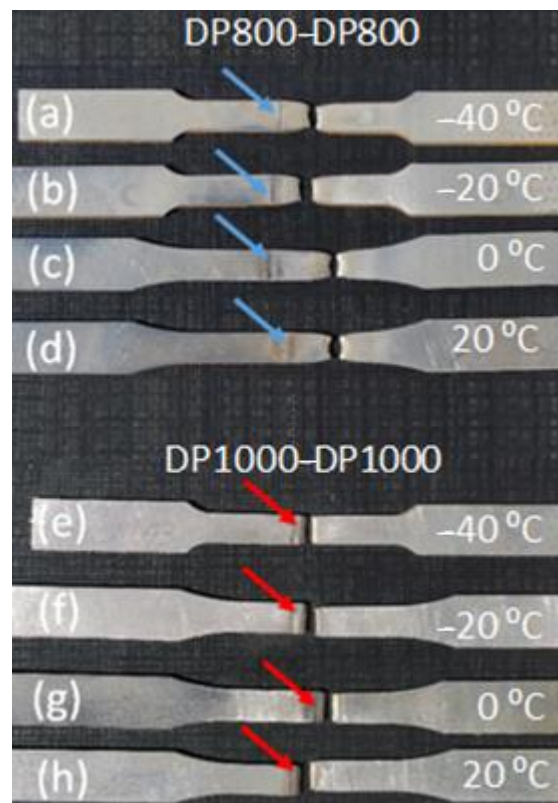
**Figure 8.** Representative fracture samples of DP800-DP800 (**a**–**d**) and DP1000-DP1000 (**e**–**h**) between testing temperatures of −40 °C and 20 °C.

Irrespective of the deformation temperatures, all DP800-welded joints fractured in the base metal as shown by the blue arrows (Figure 8a–d while all DP1000-welded joints fractured in the SCHAZ as indicated by the red arrows in Figure 8d–g. This indicates that yielding initiated from the soft zone, consequently resulting in accumulation of plastic deformation in this region until the onset of failure. In the DP800-welded joint, the deformation in the HAZ is restricted by the hardened FZ, leading to the formation of stress triaxility in the HAZ, and subsequently resulting in higher strain hardening during plastic deformation compared to the base metal [63]. Thus, the onset of yielding in the DP800-welded joints commenced in the base metal and then progressed further as the loading continued. On the other hand, this deformation mechanism was reversed during the deformation of welded DP1000. At all deformation temperatures, it can be seen that the YS and the UTS of welded DP800 and DP1000 were lower compared to the respective base metal, which can be correlated to the presence of HAZ tempered martensite, as well as the partial disappearance of existing martensite [64]. It was seen that the base metals and the welded joints demonstrated a general trend of marginal increases in strength with decreasing deformation temperatures, which is correlated to the reduced mobility of dislocations at low temperatures, leading to the increase in strength [65,66], and caused by the reduced kinetic vibrations in the lattice and difficulty of dislocation glide [67,68], except at 0 °C where both the welded joints and base metals showed a significant drop in strengths. This anomaly (i.e., loss of strength) was reported to be caused by the sudden onset of stress-induced transformation–martensitic transformation, induced by the application of external stress above the martensite start temperature (M_s) [69], leading to the reduction in values of elastic slope and yield strength [70] as well as the drop in phonon drag becomes considerably more rapid than the increases in the yield strength at this temperature (i.e., 0 °C) [71].

The influence of deformation temperatures on both total elongation (TE) and uniform elongation (UE) of the base metals and the welded joints are presented in Figure 9a,b. The uniform elongation—the elongation at the onset of plastic instability (UE) and the total

elongation (TE) of the base metals exhibited divergent behaviour throughout the test temperatures (Figure 9a). In general, the TE and UE exhibited an increasing trend from room temperature before decreasing at different test temperatures (Figure 9a). For example, DP800 BM exhibited the highest TE, it increased sharply from 16% at 20 °C to the peak value (20%) at 0 °C, more than double the UE of DP800 and DP1000 BM, respectively (Figure 9a), before decreasing steeply to 6.5% at −40 °C. It is also seen that the DP800-welded joint exhibited a superior combination of TE and UE throughout the test temperatures. DP1000 base metal UE ranging between 1.5–1.9% and the DP1000-DP1000 UE ranging between 4.0–4.5% throughout the test temperatures (Figure 9b), indicating a very poor ductility. This explains why DP1000-DP1000 welds exhibited markedly lower YS (Figure 8b) and for this reason, necking occurred in DP1000-DP1000 joint after just 3% UE. However, the TE increases until it reaches 4.5% at rupture for DP1000-DP1000 welded joints (Figure 9b). It has been reported that low UE values are often a cause for concern [72], as it is usually accompanied by a low resistance to fracture under other forms of loading [73].
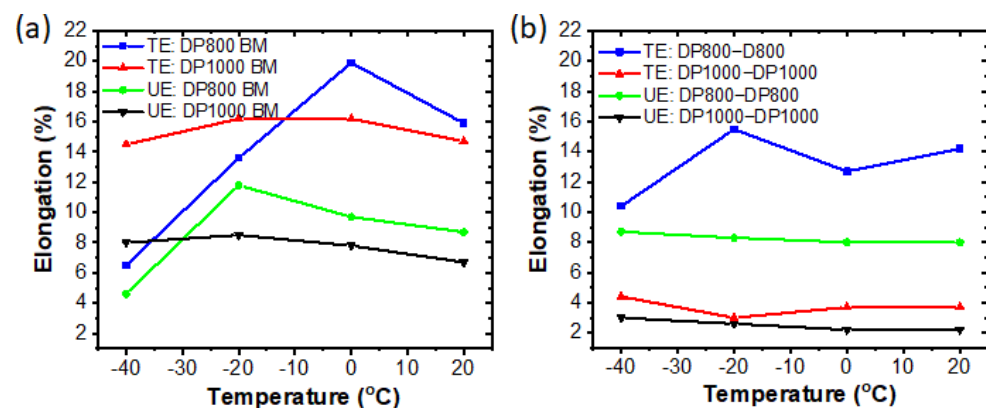
Figure 9. Elongation as a function of deformation temperatures for (**a**) DP800 and DP1000 BMs, (**b**) welded DP800 and DP1000 joints, at different deformation temperatures from 20 °C to −40 °C.

### 3.4. Work Hardening Behaviour

Strain hardening is an essential parameter for determining the surface deformation behaviour of a material. Work hardening can enhance hardness, the yield limit, as well as enhancing the material's resistance to deformation. To determine the work hardening ability of the BMs and the welded joints as well as the influence of temperature on the uniform plastic deformation, the work hardening exponent *n* in the Hollomon power law equation:

$$\sigma = K\mathcal{E}_T^n \tag{2}$$

was determined from the true stress–strain data in the uniform plastic deformation region, where *K* is the material coefficient. The calculated values of the strain hardening exponent *n* derived from the slopes of the ($\log\sigma_T$ vs. $\log\epsilon_T$) curves at different deformation temperatures are shown in Figure 10a. In general, it is evident that the base metals *n*-values estimated from the Hollomon power law equation (i.e., Equation (2)) exhibited an increasing trend with decreasing deformation temperatures except at −40 °C when the trends break down (Figure 10a). For example, both DP800 BM and DP1000 BM demonstrated an increase in *n*-values from 0.41 and 0.15, respectively, at 20 °C, respectively, before reaching a maximum value of 0.53 and 0.45, respectively, at −20 °C. It is interesting to note that DP1000 BM exhibited much lower *n*-value (0.15) compared to DP800 BM (*n*-value = 0.41) at 20 °C. Similar finding was reported by [64] for the DP980 BM (*n*-value ≈ 0.16) when investigating the tensile properties and work hardening behaviour of laser-welded dual-phase steel joints. This indicates that DP800 exhibits better deformation characteristics compared to DP1000 base metal at 20 °C, measured over plastic strain of 0.54% to 6.6%. The improved deformation of DP800 BM can be attributed to the presence of a higher volume fraction of

deformable ferrite than in the DP1000 BM. This is in agreement with the findings of [74] that increasing the volume fraction of martensite in a DP steel usually results in a decrease in *n*-value. However, DP1000 BM exhibited a slightly higher *n*-value compared to DP800 BM at −40 °C. It is noteworthy that the higher ferrite volume fraction corresponds to higher hardening capacity, and consequently higher capacity for the storage of dislocation and their interactions. Additionally, the strain hardening process begins in the ferrite phase, near the interface with martensite, this could be partly due to the development of significant residual stresses attributable to the austenite to martensite transformation, or partly caused by the incompatibility between the two phases, resulting in stress concentration in the area. Due to increasing strain hardening in this region, deformation is constrained to propagate towards the ferrite grains, as it exhibits lower resistance to hardening compared to the martensite phase.

It is noteworthy that DP800-welded joints exhibited remarkable *n*-values compared to the DP1000-welded joints (Figure 10a). Interestingly, at 20 °C, the DP800-welded joints showed a slightly higher *n*-value compared to the DP800 base metal. The reason for this can be attributed to the degraded HAZ microstructure of DP800-welded joints due to the tempering of martensite (i.e., HAZ softening) (Figure 3c), leading to an improved hardening capacity or higher dislocation storage. It has been shown that a higher value of *n* indicates that the steel exhibits a higher deformation tendency before necking (i.e., instability) [75]. This is evident in Figures 9b and 10a, where a higher *n*-value correlated to an improved ductility in the DP800 base metal. In general, the base metals *n*-values demonstrated strong temperature sensitivity, i.e., it increased markedly with decreasing deformation temperatures, whereas in the welded joints, the *n*-values exhibited only weak temperature dependence, i.e., *n*-values increased marginally with decreasing temperatures. The implication of the *n*-value is that it plays a key part in sheet metal forming. The higher the *n*-value, the greater the allowable deformation (i.e., elongation) prior to necking. Consequently, the higher the *n*-value, the greater the material's resistance to necking, resulting in the increase in the material's ability to stretch further before the onset of necking.
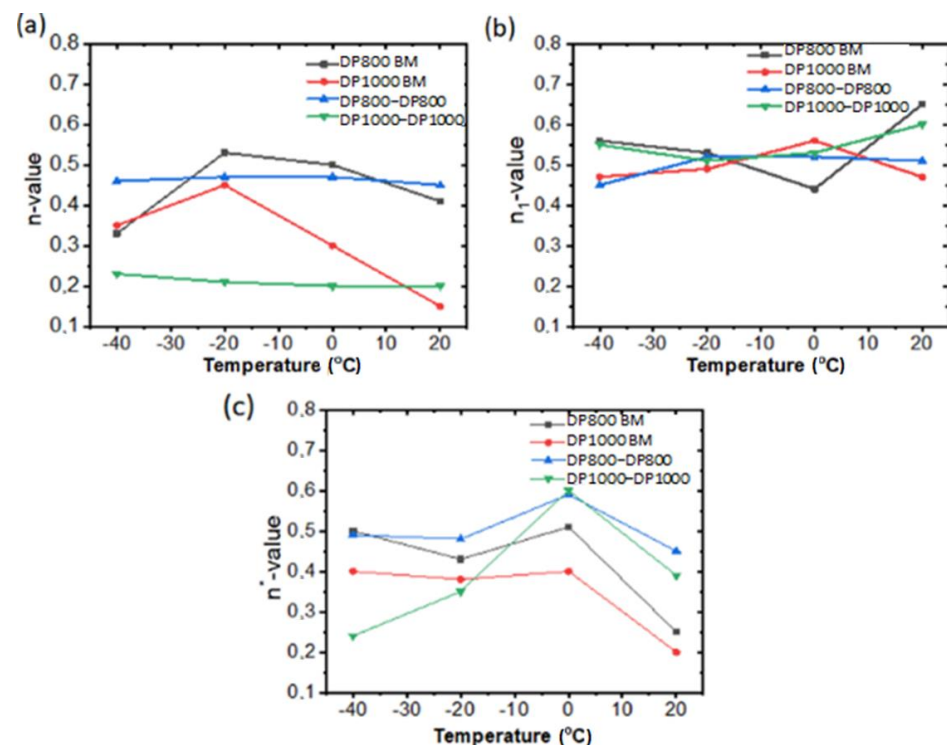
Figure 10. Strain hardening exponents based on (**a**) Hollomon equation, (**b**) C-J analysis, and (**c**) equation proposed by Afrin et al. [76] determined at different deformation temperatures for the base metals and welded joints.

To better quantify the strain-hardening characteristics of the steels, Jaoul-Crussard (C-J) plots (i.e., $\ln(d\sigma/d\epsilon)$ against $\ln\epsilon$) was plotted for the steels. The C-J analysis is based on the Ludwik equation [31]:

$$\sigma = \sigma_0 + K_1\epsilon^{n_1} \tag{3}$$

where σ_0 and $\mathcal{E}_0$ are the true stress and true strain, n_1 is the strain hardening exponent while K is the strength coefficient, representing strength increment due to strain hardening at $\mathcal{E} = 1$.

Differentiating equation (P) with respect to $\mathcal{E}$ yields:

$$\ln\frac{d\sigma}{d\epsilon} = (1 - n_1)\ln(\sigma) - \ln(kn_1)$$

The values of n_1 can be derived from the slope, $(1 - n_1)$ of the $\ln(d\sigma/d\epsilon)$ as a function of $\mathcal{E}$ curves. The different stages of work hardening behaviour can be seen from the curve of $(\ln d\sigma/d\epsilon)$ against $\ln\sigma$.

Simplifying Equation (3) yields:

$$n_1(\mathcal{E}) = \frac{d(\ln\sigma)}{d(\ln\epsilon)} \tag{4}$$

where σ is the true stress. Thus, the instantaneous n_1 value can be defined as the slope of the logarithmic stress–strain curve. The C-J plots for the base metals and welded joints are shown in Figure 9b. In general, it is seen that the hardening exponent demonstrated an increasing trend with increasing test temperature. In addition, the n values derived from the Hollomon's equation were the smallest, whereas n_1 values showed the highest while n^* values laid in-between the two. Similar findings were also observed by Afrin et al. [76].

Furthermore, it has been shown that the hardening capacity of a metal can be expressed as a ratio of the ultimate tensile strength (σ_{UTS}) to the yield strength (σ_y) [76,77]. Afrin et al. [76] remodelled the hardening capacity to a normalized variable as,

$$H_c = \frac{\sigma_{UTS} - \sigma_y}{\sigma_y} = \frac{\sigma_{UTS}}{\sigma_y} - 1 \tag{5}$$

Figure 10c presents the hardening capacity (H_c) (i.e., n^*-values) of the base metals and welded joints tested at different deformation temperatures. The n^* of the base metals and the welded joints increased with decreasing test temperatures from 20 °C to −40 °C, except for DP1000-welded joint which showed a decreasing trend between 0 °C and −40 °C. The hardening capacity in the DP800-welded samples was higher than those of the base metals as well as DP1000-DP1000 welded samples (Figure 10c). According to Equation (5), the hardening capacity of a metal is inversely related to its yield strength, which in turn is related to the grain size based on the Hall–Petch relationship [78–80]. It is noteworthy that increasing grain size normally results in a decrease in the YS (Tables 2 and 3) and subsequently increasing the hardening capacity (Figure 10c). This explains why DP800 BM and DP800-DP800 (Figure 10c) demonstrated higher hardening values (i.e., n^*-values) compared to DP1000 BM and DP1000-DP1000 welded joints (Figure 10c), while a decrease in the grain size decreases the difference of the flow resistance between the grain boundary and the interior, which ultimately reduces the hardening capacity [77]. In summary, the calculated work-hardening exponents according to the three equations were higher in the welded joints except for DP1000 welded joints that were lower at −20 °C and −40 °C, respectively (Figure 10c). It is also observed that the Hollomon exponent (n) values were the smallest while n_1 exhibited the highest values, while the values of n^* laid between those of n and n_1. These results correlate well with the findings of [76]. Additionally, the values of n exhibited increasing trends with decreasing temperatures. In general, comparison of the values of n, n_1, and n^* shows that the results obtained from Hollomon and C-J analyses were more consistent compared to that of Afrin model. However, in general, it is

significant to note that the values of strain hardening exponents were demonstrated to increase with decreasing temperatures in all the cases, with DP800 BM showing higher strain hardening exponents compared to DP1000 BM. In practical terms with regards to automotive applications, this signifies that DP800 BM exhibits better strain distribution ability (i.e., more uniform deformation distribution), improved resistance to deformation, and consequently superior formability when compared to DP1000 BM.

The trends in strain hardening rate of the BMs and the welded joints can be better evaluated by considering the instantaneous work hardening rate ($\theta = d\sigma/d\epsilon$) [81,82]. In general, the Kocks–Mecking plot of work hardening rate (θ) is commonly plotted as a function of the net flow stress ($\sigma - \sigma_y$) to evaluate the work hardening characteristics of metals and alloys [83]. The Kocks–Mecking plots at various deformation temperatures for the base metals and the welded joints are shown in Figure 11a–d. In general, it is seen that the base metals and the welded joints exhibited a similar stage III hardening, i.e., the work hardening rate (θ) decreasing almost linearly with increasing net flow stress, which is correlated to simultaneous deformation of ferrite and martensite with cross slip of dislocation and dynamic recovery of ferrite. Additionally, austenite to martensite transformation results in mobile dislocations, caused by volume expansion, which enhances initial high strain hardening rate.
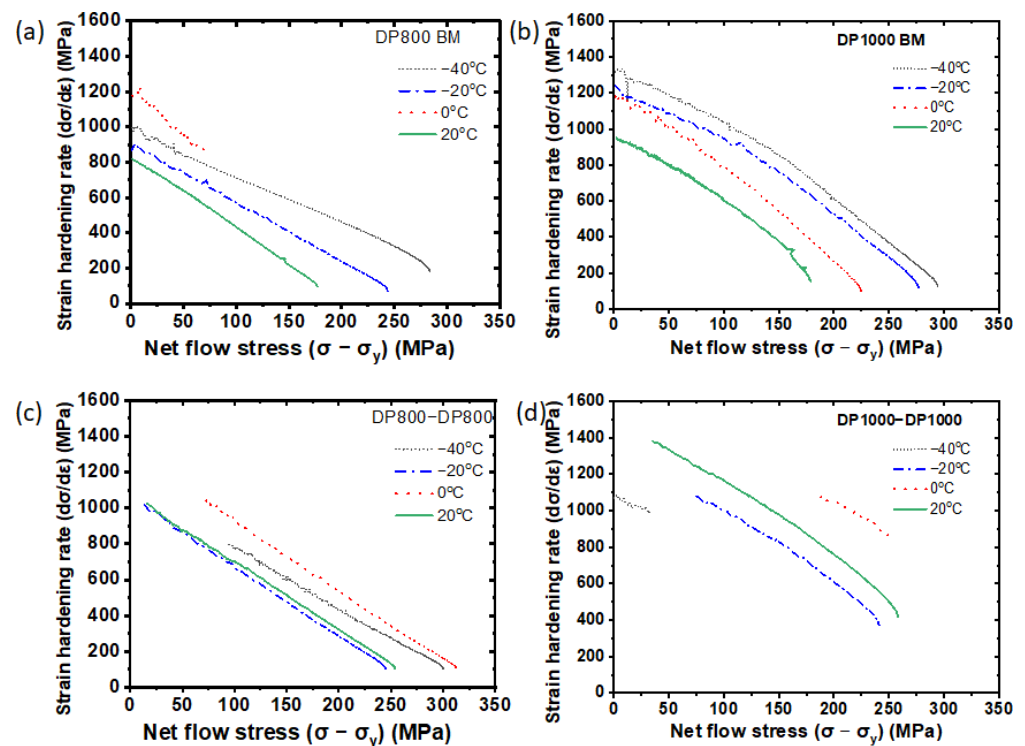
Figure 11. Strain hardening rate as a function of net flow stress for (**a**) DP800, (**b**) DP1000 BM, (**c**) DP800 welds, and (**d**) DP1000 welds, at different deformation temperatures from 20 °C to −40 °C.

In stage III, the hardening rate decreases steadily and is distinguished by a rise in the rate of loss of dislocation density, which is correlated to the steels undergoing dynamic recovery, where strain hardening rate reduces with increasing strain. In stage III, the materials are sensitive to temperature and it is assumed that the saturation stress is reached (i.e., it remains constant) [84]. This trend of linear decrease in the stage III work hardening rate is attributable to the simultaneous deformation of martensite and ferrite phases in the steels, with the accompanied cross-slip of dislocations and dynamic recovery of ferrite [27]. It has been shown by [27] that the stage III hardening rate depends on applied strain rate and deformation temperature. However, in this present study, the strain rate remained constant, but test temperatures were varied. It can be seen that at

all test temperatures, DP800 and DP1000 BM showed decreasing linear trends as shown in Figure 11a,b, i.e., θ decreased monolithically with increasing net flow stress. Further, it is observed that DP800 BM and DP1000 BM exhibited the highest strain hardening rates at test temperatures of 0 °C and −20 °C, respectively. Additionally, DP800 exhibited the shortest strain hardening rate of the two base metals at a test temperature of 0 °C (Figure 11a) while DP1000 BM exhibited the overall highest strain hardening rate, and which occurred at −20 °C (Figure 11a). Overall, DP1000 BM appeared to show an improved strain hardening rate compared to DP800 BM with regards to the net flow stress. The higher strain hardening rate of DP1000 BM can be attributed to the higher volume fraction of martensite [85,86].

Again, similar to the trends observed in the base metals, the welded joints also showed the presence of only stage III hardening at all test temperatures (Figure 11b,c). In addition, when compared to the base metals (Figure 10a,b), the welded joint exhibited a decrease in work hardening rate with increasing temperatures (Figure 11c,d). The single-stage of strain hardening behaviour (stage III hardening), i.e., the linear decrease in work hardening rate demonstrated by the base metals can be correlated to the simultaneous deformation of both martensite and ferrite with the accompanied cross slip of dislocations and dynamic recovery of ferrite [18,23,87]. Furthermore, similar to the base metals trends, the welded joints also exhibited a high initial strain hardening rate. The reason for this trend in the base metals is that austenite to martensite phase transformation results in mobile dislocations, caused by volume expansion, thus contributing to an initial high strain hardening rate [26]. The highest and lowest strain hardening rate for DP800-welded joints occurred at 0 °C and −20 °C, respectively. In contrast, DP1000-welded joints showed the highest hardening rate at 0 °C and the minimum work hardening at −20 °C. It is noteworthy that DP1000-welded joints also demonstrated the smallest flow stress at −40 °C (Figure 11d). Furthermore, DP1000-welded joints exhibited a higher work hardening rate when compared to that of DP800-welded joints (Figure 11b,c). In summary, an important observation on the effect of deformation temperatures on the welded joints showed a decreasing trend in work hardening rate with increasing temperatures (Figure 10c,d).

3.5. Fractography

Figure 12a–d shows the characteristic tensile fracture surfaces of DP800- and DP1000-welded joints at different deformation temperatures. It was observed that the base metals and the welded joints exhibited similar characteristics. In general, the fractures were located in the base metal of DP800 welded joints Figure 8a–d, while in the welded DP1000 welds, the fractures were located in the tempered HAZ (i.e., softened zone) (Figure 8e–h), as discussed in Section 3.3, and all the samples exhibited predominantly ductile fracture as shown in Figure 12a–d. In general, it is seen from the SEM image in Figure 12 that the fracture surfaces of the welded joints exhibited predominantly microvoids. Microvoids can be correlated with decohesion of the ferrite–martensite interface or segregation of adjoining particles caused by local deformation generated within the ductile region. This indicates that even the deformation behaviour of the tempered martensite region (SCHAZ) of DP1000 with the inherent ferrite matrix and precipitated carbides exhibited dimple morphology (Figure 12c,d). This is a desired fracture mode, as significant amounts of plastic deformation could absorb impact energy during crash, and consequently improving crashworthiness. However, the fracture surfaces of both DP800- and DP1000 welded joints exhibited extensive fibrous areas, predominantly by micro-void coalescence. However, some isolated cleavage areas were observed Figure 12a–d.
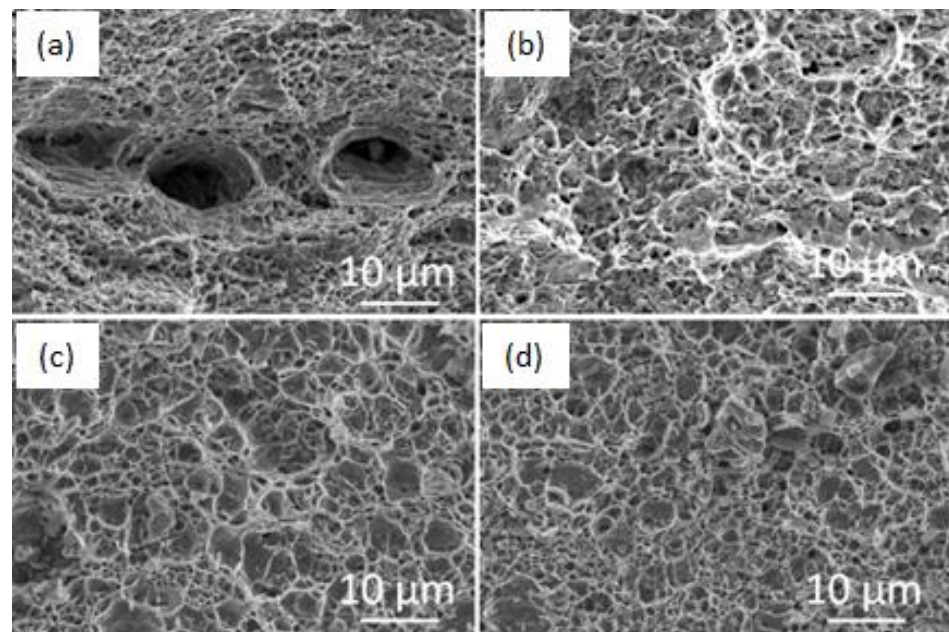
Figure 12. Representative SEM images of tensile fracture surfaces of the DP800-welded joints tested at deformation temperature of (**a**) −40 °C (**b**) 0 °C; DP1000-welded joints tested at deformation temperature of (**c**) −40 °C, and (**d**) 0 °C.

A careful analysis of the SEM images revealed that the dimple sizes on the fracture surface of the DP800-welded joints (Figure 12a,b) were slightly larger compared to those of the DP1000-welded joints (Figure 12c,d). The explanation for this is that the amount of deformable ferrite is higher in DP800-welded joints compared to DP1000-welded joints, resulting in a larger elongation than the DP1000-welded joints (Figure 9a,b). In addition, as mentioned earlier, the measured ductility (total elongation) of the welded joints improved marginally from 20 °C to −20 °C, before decreasing slightly at −40 °C (Figure 8b) which correlated with the larger sizes of dimple sizes at 0 °C compared to those at −40 °C as shown in Figure 12a–d. In summary, although the deformation of the steels were performed at sub-zero temperatures, the fractured base metals and the weld joints demonstrated characteristics of a ductile fracture with the attendant microplastic deformation, void nucleation, and subsequent void growth caused by plastic flow of the matrix during plastic deformation as well as microvoids coalescence due to the linking together of adjacent voids, which leads to necking and ultimately results in fracture.

4. Conclusions

A detailed data analysis of flow curves of laser-welded DP800 and DP1000 steel joints tested between deformation temperatures of −40 °C and 20 °C resulted in the following major conclusions:

1. DP800 and DP1000 were joined using Nd:YAG laser welding. The results showed that the fusion zone (FZ) consisted of a full martensitic structure compared to the base metals due to fast cooling associated with laser welding, resulting in a significant FZ hardness. However, softening was observed in the HAZ of the welded joints which was correlated to the partial disappearance and tempering of the pre-existing martensite in the base metal microstructures. The degree of softening and the width of the softened region were higher in the DP1000-welded joints than in the welded DP800 joints.

2. The UTS of welded DP800 and DP1000 increased between 1.5–2.7% and 1.6–5.5%, respectively, and work-hardening exponent of the welded joints increased slightly while the strain-hardening capacity of the base metals was much higher than those of the welded joints with decreasing temperatures. The welded joints and the base metals

demonstrated only stage III strain hardening, with DP800-welded joints exhibited excellent uniform and total elongation ranging between 8.0–8.7% and 10.4–14.2%.

3. The *n*-values of DP800-welded joints were remarkably higher compared to that of DP1000-welded joints. Further, the DP800-welded joints showed a slightly higher *n*-value at 20 °C compared to the DP800 base metal due to HAZ softening in the welded joint.

4. The welded joints of DP1000-DP10000 steel exhibited a higher work hardening rate when compared to that of DP800-DP800-welded joints. The highest and lowest strain hardening rate for DP800-DP800 joints occurred at 0 °C and −20 °C, respectively. In contrast, DP1000-DP1000 showed the highest hardening rate at 0 °C and the minimum work hardening at −20 °C.

5. The fracture was located in all the welded joints at all deformation temperatures in the softened heat affected zone (HAZ) near the weld, and the fracture surfaces demonstrated characteristic dimple fracture.

6. The application of these findings in the automotive industry would help to provide needed data on tensile behaviour of welded DP steels at low temperatures and provide recommendations on how these properties can be optimized to ensure safe design of vehicles for low temperature applications.

References

1. Chen, H.C.; Cheng, G.H. Effect of Martensite Strength on the Tensile Strength of dual phase Steel. *J. Mater. Sci.* **1989**, *24*, 1991–1994. [CrossRef]
2. Bleck, W. Cold rolled high strength sheet steels for auto applications. *J. Miner. Met. Mater. Soc.* **1996**, *48*, 26–30. [CrossRef]
3. Rashid, M.S. Relationhsip between Steel Microstructure and Formability. In *Formable HSLA and Dual-Phase Steels: Proceedings of a Symposium*; Davenport, A.T., Ed.; Metallurgical Society of AIME: New York, NY, USA, 1977; pp. 1–24.
4. Choi, S.H.; Kim, E.Y.; Woo, W.; Han, S.H.; Kwak, J.H. The Effect of Crystallographic Orientation on the Micromechanical Deformation Tension and Failure Behaviors of DP980 Steel During Uniaxial Tension. *Int. J. Plast.* **2013**, *45*, 85–102. [CrossRef]
5. Pierman, A.P.; Bouaziz, O.; Pardoen, T.; Jacques, P.J.; Brassart, L. The Influence of Microstructure and Composition on the Plastic Behaviour of Dual-Phase Steels. *Acta Mater.* **2014**, *73*, 298–311. [CrossRef]
6. Coates, G. *Advanced High-Strength Steels Application Guidelines*; World Auto Steel: Brussels, Belgium, 2014.
7. Sodjit, S.; Uthaisangsuk, V. Microstructure based prediction of strain hardening behavior of dual phase steels. *Mater. Des.* **2012**, *41*, 370–379. [CrossRef]
8. Callister, D.W. *Materials Science and Engineering an Introduction*, 7th ed.; John Wiley & Sons, Inc.: New York, NY, USA, 2007.
9. Krauss, G. Strengthening Mechanisms in Steels. *Encycl. Mater. Sci. Technol.* **2001**, 8870–8881. [CrossRef]
10. Ghassemi-Armaki, H.; Maaß, R.; Bhat, S.P.; Sriram, V.; Greer, J.R.; Kumar, K.S. Deformation Response of Ferrite and Martensite in a Dual-Phase Steel. *Acta Mater.* **2014**, *62*, 197–211. [CrossRef]
11. Wangn, W.; Wei, X. The Effect of Martensite Volume and Distribution on Shear Fracture Propagation of 600–1000 MPa Dual Phase Sheet Steels in the Process of Deep Drawing. *Int. J. Mech. Sci.* **2013**, *67*, 100–107. [CrossRef]

12. Khorasani, M.; Ghasemi, A.H.; Rolfe, B.; Gibson, I. Additive manufacturing a powerful tool for the aerospace industry. *Rapid Prototyp. J.* **2022**, *28*, 87–100. [CrossRef]
13. Ma, C.; Chen, D.L.; Bhole, S.D.; Boudreau, G.; Lee, A.; Biro, E. Microstructure and fracture characteristics of spot-welded DP600 steel. *Mater. Sci. Eng. A* **2008**, *485*, 334–346. [CrossRef]
14. Lee, J.H.; Park, S.H.; Kwon, H.S.; Kim, G.S.; Lee, C.S. Tungsten Inert Gas, and Metal Active Gas Welding of DP780 Steel: Comparison of Hardness, Tensile Properties and Fatigue Resistance. *Mater. Des.* **2014**, *64*, 559–565. [CrossRef]
15. Huang, T.; Sato, Y.S.; Kokawa, H.; Miles, M.P.; Kohkonen, K.; Siemssen, B.; Steel, R.J.; Packer, S. Microstructural Evolution of DP980 Steel During Friction Bit Joining. *Metall. Mater. Trans. A* **2009**, *30*, 2994–3000. [CrossRef]
16. Němeček, S.; Mužík, T.; Míšek, M. Differences between laser and arc welding of HSS steels. *Phys. Procedia* **2012**, *39*, 67–74. [CrossRef]
17. Uemori, R.; Fujioka, M.; Inoue, T.; Minagawa, M.; Ichikawa, K.; Shirahata, H.; Nose, T. Steels for marine transportation and construction. *Tech. Rev.* **2012**, *391*, 37–47.
18. Bag, A.; Ray, K.K.; Dwarakadasa, E.S. Influence of martensite content and morphology on tensile and impact properties of high-martensite dual-phase steels. *Metall. Mater. Trans. A* **1999**, *30*, 1193–1202. [CrossRef]
19. Ahmad, E.; Manzoor, T.; Ali, K.L.; Akhter, J.I. Effect of Microvoid Formation on the Tensile Properties of Dual-Phase Steel. *J. Mater. Eng. Perform.* **2000**, *9*, 306–310. [CrossRef]
20. Huh, J.; Huh, H.; Lee, C.S. Effect of Strain Rate on Plastic Anisotropy of Advanced High Strength Steel. *Int. J. Plast.* **2013**, *44*, 23–46. [CrossRef]
21. Kim, J.H.; Kim, D.; Han, H.N.; Barlat, F.; Lee, M.G. Strain Rate Dependent Tensile Behavior of Advanced High Strength Steels: Experiment and Constitutive Modeling. *Mater. Sci. Eng. A* **2013**, *559*, 222–231. [CrossRef]
22. Erdogan, M. The Effect of New Ferrite Content on the Tensile Fracture Behaviour of Dual Phase Steels. *J. Mater. Sci.* **2002**, *37*, 3623–3630. [CrossRef]
23. Das, D.; Chattopadhyay, P.P. Influence of Martensite Morphology on the Work-Hardening Behavior of High Strength Ferrite-Martensite Dual-Phase Steel. *J. Mater. Sci.* **2009**, *44*, 2957–2965. [CrossRef]
24. Byun, T.S.; Kim, I.S. Tensile Properties and Inhomogeneous Deformation of Ferrite-Martensite Dual-Phase Steels. *J. Mater. Sci.* **1993**, *28*, 2923–2932. [CrossRef]
25. Akbarpour, M.R.; Ekrami, A. Effect of Temperature on Flow and Work Hardening Behavior of High Bainite Dual Phase (HBDP) Steels. *Mater. Sci. Eng. A* **2008**, *475*, 293–298. [CrossRef]
26. Jia, Q.; Guo, W.; Peng, P.; Li, M.; Zhu, Y.; Zou, G. Microstructure- and Strain Rate-Dependent Tensile Behavior of Fiber Laser-Welded DP980 Steel Joint. *J. Mater. Eng. Perform.* **2016**, *252*, 668–676. [CrossRef]
27. Kocks, U.F.; Mecking, H. Physics and phenomenology of strain hardening: The FCC case. *Prog. Mater. Sci.* **2003**, *48*, 171–273. [CrossRef]
28. Hollomon, J.H. Tensile Deformation. *Am. Inst. Min. Metall. Eng. Trans. Iron Steel Div.* **1945**, *162*, 268–289.
29. Jaoul, B. Etude de Plasticite et Application oux Meatux. *J. Mech. Phys. Solid.* **1957**, *5*, 95–114. [CrossRef]
30. Crussard, C. Relationship Between Exact Form of Tensile Curves of Metals and Accompanying Changes in Their Structure. *Rev. Met.* **1953**, *50*, 697–710. [CrossRef]
31. Ludwik, P. *Elements of Technical Mechanics*; Springer: Berlin/Heidelberg, Germany, 1909.
32. Swift, H.W. Plastic Instability Under Plane Stress. *J. Mech. Phys. Solid.* **1952**, *1*, 1–18. [CrossRef]
33. Monteiro, S.N.; Reed-Hill, R. On the double-n behaviour of iron. *Metall. Mater. Trans. B* **1971**, *2*, 2947–2948. [CrossRef]
34. Ramos, L.F.; Matlock, D.K.; Krauss, G. On the Deformation Behavior of Dual-Phase Steels. *Metall. Trans. A* **1979**, *10*, 259–261. [CrossRef]
35. Samuel, F.H. Tensile Stress-Strain Analysis of Dual-Phase Structures in a Mn-Cr-Si Steel. *Mater. Sci. Eng.* **1987**, *92*, l1–l4. [CrossRef]
36. Jha, B.K.; Avtar, R.; Dwivedi, V.S.; Ramaswamy, V. Applicability of Modified Crussard-Jaoul Analysis on the Deformation Behaviour of Dual-Phase Steels. *J. Mater. Sci. Lett.* **1987**, *6*, 891–893. [CrossRef]
37. Shin, H.; Ju, Y.; Choi, M.K.; Ha, D.H. Flow Stress Description Characteristics of Some Constitutive Models at Wide Strain Rates and Temperatures. *Technologies* **2022**, *10*, 52. [CrossRef]
38. Xu, J.; Cao, D.; Cui, J.; Zhang, X.; Li, G. Experimental Research on Tensile Behavior of Advanced High-Strength Steel DP600 at High Strain Rate. *J. Mater. Eng. Perform.* **2019**, *28*, 2411–2420. [CrossRef]
39. Cao, Y.; Karlsson, B.; Ahlström, J. Temperature and strain rate effects on the mechanical behavior of dual phase steel. *Mater. Sci. Eng. A* **2015**, *636*, 124–132. [CrossRef]
40. Cao, Y.; Ahlström, J.; Karlsson, B. Mechanical Behavior of a Rephosphorized Steel for Car Body Applications: E ects of Temperature, Strain Rate, and Pretreatment. *J. Eng. Mater. Technol.* **2011**, *133*, 021019. [CrossRef]
41. Waterschoot, T.; De Cooman, B.C.; De, A.K.; Vandeputte, S. Static strain aging phenomena in cold-rolled dual-phase steels. *Metall. Mater. Trans. A* **2003**, *34*, 781–791. [CrossRef]
42. Bleck, W.; Schael, I. Determination of crash-relevant material parameters by dynamic tensile tests. *Steel Res.* **2000**, *71*, 173–178. [CrossRef]
43. Morgans, S. Advanced high-Strength Steel Technologies in the 2013 Ford Fusion. In Proceedings of the Presented in Great Designs in Steel Seminar, Livonia, MI, USA, 16 May 2012.
44. He, H.; Forouzan, F.; Volpp, J.; Robertson, S.M.; Vuorinen, E. Microstructure and mechanical properties of laser-welded DP steels used in the automotive industry. *Materials* **2021**, *14*, 456. [CrossRef]

45. Li, Y.; Zhu, Z.; Tang, X.; Han, S.; Zhang, R.; Cui, H. Improvement of welding stability and mechanical properties of galvanized DP800 steel lap joint by high-speed tandem beam laser. *Opt. Laser Technol.* **2022**, *150*, 107958. [CrossRef]
46. Rocha, I.; Machado, I.; Mazzaferro, C. Mechanical and metallurgical properties of DP1000 steel square butt welded joints with GMAW. *Int. J. Eng. Technol.* **2014**, *4*, 26. [CrossRef]
47. Hertzberg, R.W.; Vinci, R.P.; Hertzberg, J.L. *Deformation and Fracture Mechanics of Engineering Materials*, 5th ed.; John Wiley and Sons, Inc.: Hoboken, NJ, USA, 2013.
48. Partridge, P.; Bowen, A. Limitations of the Hollomon strain-hardening equationt. *J. Appl. Phys.* **1974**, *7*, 969–978.
49. LeMaitre, J. *Handbook of Materials Behavior Models*, 1st ed.; Academic Press: Paris, France, 2001.
50. Kohnke, P. *ANSYS Theory Reference—Release 5.6*; SAS IP Inc.: Canonsburg, PA, USA, 1999.
51. Bassini, E.; Sivo, A.; Ugues, D. Assessment of the Hardening Behavior and Tensile Properties of a Cold-Rolled Bainitic–Ferritic Steel. *Materials* **2021**, *14*, 6662. [CrossRef]
52. Colla, V.; De Sanctis, M.; Dimatteo, A.; Lovicu, G.; Solina, A.; Valentini, R. Strain Hardening Behavior of Dual-Phase Steels. *Metall. Mater. Trans. A* **2009**, *40*, 2557–2567. [CrossRef]
53. Soares, G.C.; Gonzalez, B.M.; Santos, L.D.A. Strain hardening behavior and microstructural evolution during plastic deformation of dual phase, non-grain oriented electrical and AISI 304 steels. *Mater. Sci. Eng. A* **2017**, *684*, 577–585. [CrossRef]
54. Garde, A.M. *An Analysis of the Stress-Strain Behavior of Several Grades of Polycrystalline Titanium and Zirconium with Reference to Dynamic Strain Aging and Deformation Twinning between 77 and 1000 °K*; University of Florida: Gainesville, FL, USA, 1973.
55. Yurioka, N.; Kasuya, T. A chart method to determine necessary preheat in steel welding. *Weld. World* **1995**, *35*, 327–334. [CrossRef]
56. Krüger, L.; Wolf, S.; Martin, U.; Martin, S.; Scheller, P.R.; Jahn, A.; Weiß, A. The influence of martensitic transformation on mechanical properties of cast high alloyed CrMnNi-steel under various strain rates and temperatures. *J. Phy. Conf. Ser.* **2010**, *240*, 012098. [CrossRef]
57. *ASTM E92-17*; Standard Test Methods for Vickers Hardness and Knoop Hardness of Metallic Materials. ASTM International: West Conshohocken, PA, USA, 2017.
58. Biro, E.; McDermid, J.R.; Embury, J.D.; Zhou, Y. Softening kinetics in the subcritical heat-affected zone of dual-phase steel welds. *Metall. Mater. Trans. A Phys. Metall. Mater. Sci.* **2010**, *41*, 2348–2356. [CrossRef]
59. Xia, M.; Biro, E.; Tian, Z.; Zhou, Y.N. Effects of heat input and martensite on HAZ softening in laser welding of dual phase steels. *ISIJ Int.* **2008**, *48*, 809–814. [CrossRef]
60. Farabi, N.; Chen, D.L.; Li, J.; Zhou, Y.; Dong, S.J. Microstructure and Mechanical Properties of Laser Welded DP600 Steel Joints. *Mater. Sci. Eng. A* **2010**, *527*, 1215–1222. [CrossRef]
61. Xia, M.S.; Kuntz, M.L.; Tian, Z.L.; Zhou, Y. Failure study on laser welds of dual phase steel in formability testing. *Sci. Technol. Weld. Join.* **2008**, *13*, 378–387. [CrossRef]
62. Saha, D.C.; Westerbaan, D.; Nayak, S.S.; Biro, E.; Gerlich, A.P.; Zhou, Y. Materials Science & Engineering A Microstructure-properties correlation in fi ber laser welding of dual-phase and HSLA steels. *Mater. Sci. Eng. A* **2014**, *607*, 445–453. [CrossRef]
63. Parkes, D.; Xu, W.; Westerbaan, D.; Nayak, S.S.; Zhou, Y.; Goodwin, F.; Bhole, S.; Chen, D.L. Microstructure and fatigue properties of fiber laser welded dissimilar joints between high strength low alloy and dual-phase steels. *Mater. Des.* **2013**, *51*, 665–675. [CrossRef]
64. Panda, S.K.; Sreenivasan, N.; Kuntz, M.L.; Zhou, Y. Numerical Simulations and Experimental Results of Tensile Test Behavior of Laser Butt Welded DP980 Steels. *J. Eng. Mater. Technol.* **2008**, *13*, 041003. [CrossRef]
65. Farabi, N.; Chen, D.L.; Zhou, Y. Tensile properties and work hardening behavior of laser-welded dual-phase steel joints. *J. Mater. Eng. Perform.* **2012**, *21*, 222–230. [CrossRef]
66. Dowling, N. *Mechanical Behavior of Materials: Engineering Methods for Deformation*, 4th ed.; Prentice-Hall International: Englewood Cliffs, NJ, USA, 2012.
67. Parkes, D.; Westerbaan, D.; Nayak, S.S.; Zhou, Y.; Goodwin, F.; Bhole, S.; Chen, D. Tensile properties of fiber laser welded joints of high strength low alloy and dual-phase steels at warm and low temperatures. *Mater. Des.* **2014**, *56*, 193–199. [CrossRef]
68. Dieter, G.E.E. *Mechanical Metallurgy*, 3rd ed.; Metric, S.I., Ed.; McGraw-Hill: London, UK, 1988.
69. Gurrutxaga-Lerma, B.; Shehadeh, M.A.; Balint, D.S.; Dini, D.; Chen, L.; Eakins, D.E. The effect of temperature on the elastic precursor decay in shock loaded FCC aluminium and BCC iron. *Int. J. Plast.* **2017**, *96*, 135–155. [CrossRef]
70. Sakamoto, H. Distinction between thermal and stress-induced martensitic transformations and inhomogeneity in internal stress. *Mater. Trans.* **2002**, *43*, 2249–2255. [CrossRef]
71. Aderibigbe, I.; Popoola, P.; Sadiku, R.; Biro, E. Influence of low temperatures on mechanical behavior of laser welded dual phase steels Influence of low temperatures on mechanical behavior of laser welded dual phase steels. *J. Laser Appl.* **2022**, *34*, 022011. [CrossRef]
72. Konings, R.; Allen, T.R.; Stoller, R.E. Basic Aspects of Radiation Effects in Solids/Basic Aspects of Multi-Scale Modeling. In *Comprehensive Nuclear Materials*; Elsevier: Madrid, Spain, 2012; p. 486.
73. Davis, J.R. Introduction to tensile testing. In *Tensile Testing*; ASM International: Materials Park, OH, USA, 2004; pp. 1–12.
74. Kumar, A.; Singh, S.B.; Ray, K.K. Influence of bainite/martensite-content on the tensile properties of low carbon dual-phase steels. *Mater. Sci. Eng. A* **2008**, *474*, 270. [CrossRef]
75. Movahed, P.; Kolahgar, S.; Marashi, S.P.H.; Pouranvari, M.; Parvin, N. The Effect of Intercritical Heat Treatment Temperature on the Tensile Properties and Work Hardening Behavior of Ferrite-Martensite Dual Phase Steel Sheets. *Mater. Sci. Eng. A* **2009**, *518*, 1–6. [CrossRef]

76. Afrin, N.; Chen, D.L.; Cao, X.; Jahazi, M. Strain hardening behavior of a friction stir welded magnesium alloy. *Scr Mater* **2007**, *57*, 1004–1007. [CrossRef]
77. Luo, J.; Mei, Z.; Tian, W.; Wang, Z. Diminishing of work hardening in electroformed polycrystalline copper with nano-sized and uf-sized twins. *Mater. Sci. Eng. A* **2006**, *441*, 282–290. [CrossRef]
78. Ligda, J.P. Effects of Grain Size on the Quasi-Static Mechanical Properties of Ultrafine-Grained and Nanocrystalline Tantalum. PhD Thesis, The University of North Carolina at Charlotte, Charlotte, NC, USA, 2013.
79. Dieter, G.E. *Mechanical Metallurgy*, 3rd ed.; McGraw-Hill: New York, NY, USA, 1986.
80. Hosford, W.F. *Mechanical Behavior of Materials*; Cambridge University Press: New York, NY, USA, 2005.
81. Christopher, J.; Choudhary, K.; Isaac Samuel, E.; Srinivasan, V.S.; Mathew, M.D. Tensile flow and work hardening behaviour of9Cr-1Mo ferritic steel in the frame work of Voce relationship. *Mater. Sci. Eng. A* **2011**, *528*, 6589–6595. [CrossRef]
82. Mecking, H.; Kocks, U.F. Kinetics of flow and strain-hardening. *Acta Metall.* **1981**, *29*, 1865–1875. [CrossRef]
83. Chowdhury, S.M.; Chen, D.L.; Bhole, S.D.; Cao, X.; Powidajko, E.; Weckman, D.C.; Zhou, Y. Tensile properties and strain-hardeningbehavior of double-sided arc welded and friction stir welded AZ31B magnesium alloy. *Mater. Sci. Eng. A* **2010**, *527*, 2951–2961. [CrossRef]
84. Humphreys, F.J.; Roher, G.S.; Rollett, A. The Deformed State. In *Recrystallization and Related Annealing Phenomena*, 3rd ed.; Elsevier: Oxford, UK, 2017; pp. 21–23.
85. Rana, A.K.; Paul, S.K.; Dey, P.P. Effect of martensite volume fraction on cyclic plastic deformation behavior of dual phase steel: Micromechanics simulation study. *J. Mater. Res. Technol.* **2019**, *8*, 3705–3712. [CrossRef]
86. Birgani, E.N.; Pouranvari, M. Effect of martensite volume fraction on the work hardening behavior of dual phase steels. *Proc. Metal* **2009**, *2009*, 19–21.
87. Zhang, J.; Di, H.; Deng, Y.; Misra, R.D.K. Effect of martensite morphology and volume fraction on strain hardening and fracture behavior of martensite–ferrite dual phase steel. *Mater. Sci. Eng. A* **2015**, *627*, 230–240. [CrossRef]